Quantitative PET Imaging of Tumor Integrin $\alpha_v\beta_3$ Expression with ^{18}F-FRGD2

Xianzhong Zhang, PhD; Zhengming Xiong, MD, PhD; Yun Wu, PhD; Weibo Cai, PhD; Jeffery R. Tseng, MD; Sanjiv S. Gambhir, MD, PhD; and Xiaoyuan Chen, PhD

Molecular Imaging Program at Stanford (MIPS), and Bio-X Program, Department of Radiology, Stanford University, Stanford, California

The development of noninvasive methods to visualize and quantify integrin $\alpha_v\beta_3$ expression in vivo appears to be crucial for the success of antiangiogenic therapy based on integrin antagonism. Precise documentation of integrin receptor levels will allow appropriate selection of patients who will most likely benefit from an antiintegrin treatment regimen. Imaging can also be used to provide an optimal dosage and time course for treatment based on receptor occupancy studies. In addition, imaging integrin expression will be important to evaluate antiintegrin treatment efficacy and to develop new therapeutic drugs with favorable tumor targeting and in vivo kinetics. We labeled the dimeric RGD peptide E[c(RGDyK)]$_2$ with ^{18}F and evaluated its tumor-targeting efficacy and pharmacokinetics of ^{18}F-FB–E[c(RGDyK)]$_2$ (^{18}F-FRGD2). **Methods:** E[c(RGDyK)]$_2$ was labeled with ^{18}F by conjugation coupling with *N*-succinimidyl-4-^{18}F-fluorobenzoate (^{18}F-SFB) under a slightly basic condition. The in vivo metabolic stability of ^{18}F-FRGD2 was determined. The diagnostic value after injection of ^{18}F-FRGD2 was evaluated in various xenograft models by dynamic microPET followed by ex vivo quantification of tumor integrin level. **Results:** Starting with $^{18}F^-$ Kryptofix 2.2.2./K_2CO_3 solution, the total reaction time for ^{18}F-FRGD2, including final high-performance liquid chromatography purification, is about 200 $\pm$ 20 min. Typical decay-corrected radiochemical yield is 23% $\pm$ 2% (n = 20). ^{18}F-FRGD2 is metabolically stable. The binding potential extrapolated from graphical analysis of PET data and Logan plot correlates well with the receptor density measured by sodium dodecyl sulfate polyacrylamide electrophoresis and autoradiography in various xenograft models. The tumor-to-background ratio at 1 h after injection of ^{18}F-FRGD2 also gives a good linear relationship with the tumor tissue integrin level. **Conclusion:** The dimeric RGD peptide tracer ^{18}F-FRGD2, with high integrin specificity and favorable excretion profile, may be translated into the clinic for imaging integrin $\alpha_v\beta_3$ expression. The binding potential calculated from simplified tracer kinetic modeling such as the Logan plot appears to be an excellent indicator of tumor integrin density.

Key Words: molecular imaging; integrin $\alpha_v\beta_3$; dimeric RGD peptide; dynamic microPET; Logan plot

J Nucl Med 2006; 47:113–121

Cell adhesion receptors of the integrin family, which are responsible for a wide range of cell-extracellular matrix and cell–cell interactions, have been well studied in many tumor types (*1*). One of the most prominent members of this receptor class is $\alpha_v\beta_3$ integrin, which is related to several pathologic processes and is being investigated intensively (*2*). The cell adhesion molecule integrin $\alpha_v\beta_3$ is highly expressed on activated endothelial cells (endothelial cells undergo angiogenesis and vascular remodeling) and solid tumor cells, particularly in pathways stimulated by vascular endothelial growth factor (*3–5*). It is not expressed on mature vessels or on nonneoplastic epithelium. The expression of integrin $\alpha_v\beta_3$ on sprouting capillary cells and its interaction with specific matrix ligands has been shown to play a key role in angiogenesis and metastasis (*6*). The ability to noninvasively visualize and quantify $\alpha_v\beta_3$ integrin expression level will provide new opportunities to document tumor (tumor cells and sprouting tumor vasculature) receptor expression, more appropriately select patients considered for antiintegrin treatment, and monitor treatment efficacy in integrin-positive patients (*7*). Contrast-enhanced ultrasound with microbubbles targeted to α_v integrins expressed on the neovascular endothelium has been used to image tumor integrin status in addition to tumor microvascular blood volume and blood velocity, which can be easily detected with nontargeted microbubbles (*8–10*). In an animal model, Sipkins et al. (*11*) recently demonstrated that it is feasible to image $\alpha_v\beta_3$ expression using MRI and antibody-coated paramagnetic liposomes. It has also been shown that near-infrared fluorescent dye conjugated cyclic RGD peptide was able to visualize subcutaneously inoculated integrin-positive tumors (*12,13*). To date, most of the studies have been focused on developing suitably radiolabeled small RGD peptide antagonists of $\alpha_v\beta_3$ as radiopharmaceuticals for SPECT and PET imaging applications (*7,14*).

For radionuclide imaging of integrin expression in vivo, the tumor-targeting efficacy and in vivo kinetic profile are highly related to the receptor-binding affinity and specificity, hydrophilicity, molecular size, and overall molecular charge of the resulting radiotracer. Initial studies with ^{18}F-labeled monomeric RGD peptides indicated moderate

Received Jun. 14, 2005; revision accepted Sep. 19, 2005.

For correspondence or reprints contact: Xiaoyuan Chen, PhD, Department of Radiology, 1201 Welch Rd., P095, Stanford University, Stanford, CA 94305-5484.

E-mail: shawchen@stanford.edu

initial uptake in integrin-positive tumors, but the rapid tumor washout and unfavorable hepatobiliary excretion route of this type of tracer limited their further applications, especially in an attempt to detect lesions in the lower abdomen (*15,16*). The in vivo pharmacokinetics of the monomeric RGD peptide tracers was significantly improved by incorporation of a heterofunctional sugar or poly(ethylene glycol) moiety between the RGD peptide and the ^{18}F-labeling prosthetic group (±)-2-^{18}F-fluoropropionate for RGD-containing glycopeptide (*17–19*) and 4-^{18}F-fluorobenzoyl for PEGylated RGD peptide (*20,21*). Both compounds had fast blood clearance, rapid and moderate tumor uptake, and moderate tumor washout, resulting in a high tumor-to-background ratio.

We recently found that the receptor-binding characteristics of dimeric and multimeric RGD peptides would be better than that of monomeric RGD peptide based on polyvalency (*22–25*). The receptor binding of the one RGD domain significantly enhances the local concentration of the other RGD domain in the vicinity of the receptor, which may lead to a faster rate of receptor binding or a slower rate of dissociation from the radiolabeled RGD dimer. The dimeric RGD peptide with almost 1 order of magnitude higher integrin-binding affinity than the monomeric analog is thus labeled with ^{18}F (*24*). ^{18}F-FB–E[c(RGDyK)]$_2$ (^{18}F-FRGD$_2$) showed predominant renal excretion and almost twice as much tumor uptake in the same animal model as compared with the monomeric tracer ^{18}F-FB-c(RGDyK). In this study we further evaluated this tracer in various preclinical animal models to measure the metabolic stability and to visualize and quantify integrin $\alpha_v\beta_3$ expression in vivo.

MATERIALS AND METHODS

Materials

All chemicals obtained commercially were used without further purification. Dimeric RGD peptide E[c(RGDyK)]$_2$ was synthesized as previously described (*22–25*). No-carrier-added ^{18}F-F$^-$ was obtained from PETNET Inc. The ^{18}F-F$^-$ was trapped on an anion-exchange resin and then eluted with 0.5 mL K_2CO_3 (2 mg/mL in H_2O) combined with 1 mL Kryptofix 2.2.2. (Sigma-Aldrich) (10 mg/mL in acetonitrile).

Semipreparative reversed-phase high-performance liquid chromatography (HPLC) was accomplished by using a Dionex P680 chromatography system with a UVD 170U detector and a solid-state radiation detector (model 105S; Carroll & Ramsey Associates). Purification was performed with a Vydac 218TP510 protein and peptide column (5 μm; 250 × 10 mm). The flow rate was 5 mL/min. The mobile phase was changed from 95% solvent A (0.1% trifluoroacetic acid [TFA] in water) and 5% solvent B (0.1% TFA in acetonitrile) (0–2 min) to 35% solvent A and 65% solvent B at 32 min. The analytic HPLC method was performed with the same gradient system but with a Vydac 218TP54 column (5 μm; 250 × 4.6 mm) and a flow rate of 1 mL/min. The absorbance was monitored at 218 nm. Reversed-phase extraction C_{18} Sep-Pak cartridges (Waters) were pretreated with methanol and water before use.

Radiochemistry

We have previously reported the synthesis of ^{18}F-FB–E[c(RGDyK)]$_2$ (^{18}F-FRGD$_2$) (*24*). In this study we systemically investigated the effect of pH, temperature, and reaction time on the coupling yield between *N*-succinimidyl-4-^{18}F-fluorobenzoate (^{18}F-SFB) and dimeric RGD peptide E[c(RGDyK)]$_2$. In brief, ^{18}F-SFB was purified by semipreparative HPLC. The appropriate fractions were collected and diluted with water and trapped by a C_{18} cartridge. The cartridge was then washed with water and blown dry with argon. ^{18}F-SFB was reeluted with acetonitrile and rotary evaporated to dryness. The dried ^{18}F-SFB was then redissolved in dimethyl sulfoxide (200 μL) and added to the E[c(RGDyK)]$_2$ (200 μg, 0.15 μmol) dissolved in sodium phosphate buffer (800 μL). Final purification was accomplished by semipreparative HPLC. The HPLC fractions containing the activity was then combined and evaporated with a stream of argon to remove acetonitrile. The pH of the resulting aqueous solution was adjusted to 7.0 with 0.1N NaOH and passed through an activated Waters C_{18} Sep-Pak cartridge, washed with water, and eluted with 200-μL portions of 80% ethanol. The ethanol fractions were pooled and evaporated to a small volume. The activity was finally reconstituted in phosphate-buffered saline (PBS) and passed through a 0.22-μm Millipore filter into a sterile multidose vial for in vivo applications.

Cell Lines

Six cell lines were used for in vitro and in vivo experiments. All cells were obtained from the American Type Culture Collection and all culture media were obtained from Invitrogen Co. (GIBCO). U87MG glioblastoma cells were grown in Dulbecco's modified Eagle medium (DMEM, low glucose), MDA-MB-435 breast cancer carcinoma cells were grown in Leibovitz's L15 medium, C6 rat glioma cells were grown in DMEM (high glucose), PC-3 prostate adenocarcinoma and A549 lung carcinoma cells were grown in F-12K nutrient mixture (Kaighn's modification), and NCI-H1975 non–small cell lung cancer cells were grown in RPMI 1640 medium. All cell lines were cultured in the medium supplemented with 10% (v/v) fetal bovine serum at 37°C.

Radioligand-Binding Measurements

U87MG, MDA-MB-435, C6, PC-3, A549, and NCI-H1975 cell lines were grown as described. ^{125}I-Echistatin (specific activity, 74 TBq/mmol) was purchased from Amersham. For cell receptor assay studies, Millipore 96-well filter plates were added with different concentrations (0–100 nmol/L) of echistatin in binding buffer (20 mmol/L Tris, 150 mmol/L NaCl, 2 mmol/L $CaCl_2$, 1 mmol/L $MgCl_2$, 1 mmol/L $MnCl_2$, 0.10% bovine serum albumin, pH 7.4), and 555 Bq ^{125}I-echistatin (in 50 μL binding buffer) in each well. The cells in 50-μL suspension (2×10^5 cells/well) were seeded and the total volume for each well was adjusted to 200 μL with binding buffer. The mixture was incubated for 2 h by shaking at room temperature. At the end of the incubation period, the cells were filtered with the use of a Millipore Multiscreen vacuum manifold and washed twice with cold binding buffer. The hydrophilic polyvinylidene difluoride (PVDF) filters were then collected and the radioactivity was determined using a NaI(Tl) γ-counter (Packard Instruments Co.). Nonspecific binding was determined with 100 nmol/L of echistatin. Scatchard plots were derived by plotting bound/free ligand versus. bound ligand and the maximum number of binding sites (B_{max}) were

calculated by analyzing the data with nonlinear regression by use of GraphPad Prism software (version 4).

Animals Models

All animal experiments were performed under a protocol approved by Stanford's Administrative Panel on Laboratory Animal Care. The MDA-MB-435 breast cancer model was established by orthotopic injection of 5×10^6 cells into the left mammary fat pad. The PC-3 prostate cancer model was obtained by injecting a mixture of 5×10^6 cells suspended in 50 μL F-12K medium and 50 μL Matrigel (BD BioSciences) into the right front leg of male athymic nude mice. The other 4 tumor models (U87MG, C6, NCI-H1975, and A549) were established in a way similar to that of the PC-3 model except that female nude mice were used. The mice were used for microPET studies when the tumor volume reached 300–400 mm^3 (2–3 wk after inoculation for NCI-H1975 and C6; 3–4 wk after inoculation for U87MG, MDA-MB-435, PC-3, and A549). Three mice were used for each tumor models.

Metabolic Stability

Nude mice bearing U87MG tumors were intravenously injected with 37 MBq of ^{18}F-FRGD2. The animals were sacrificed and dissected 60 min after tracer injection. Blood, urine, liver, kidneys, and tumor were collected. Blood was immediately centrifuged for 5 min at 13,200 rpm. Organs were homogenized using an IKA Ultra-Turrax T8 (IKA Works Inc.), suspended in 1 mL of PBS, pH 7.4, and centrifuged for 5 min at 13,200 rpm. After removal of the supernatants, the pellets were washed with 500 μL of PBS. For each sample supernatants of both centrifugation steps were combined and passed through Sep-Pak C_{18} cartridges. The urine sample was directly diluted with 1 mL of PBS and then passed through a Sep-Pak C_{18} cartridge. The cartridges were washed with 2 mL of water and eluted with 2 mL of acetonitrile containing 0.1% TFA. The combined aqueous and organic solutions were concentrated to about 1 mL by rotary evaporation. The residues were passed through a 0.22-μm Millipore filter and then injected onto an analytic HPLC column using a flow rate of 1 mL/min and a gradient as described. Radioactivity was monitored using a solid-state radiation detector. At the same time, the eluent was also collected by a fraction collector (0.5 min/fraction) and the activity of each fraction was measured with the γ-counter. The HPLC analysis was performed in duplicate and the extraction efficiency was determined in triplicate.

microPET

PET was performed using a microPET R4 rodent model scanner (Concorde Microsystems Inc.). The scanner has a computer-controlled bed and 10.8-cm transaxial and 8-cm axial fields of view (FOVs). It has no septa and operates exclusively in the 3-dimensional list mode. Animals were placed near the center of the FOV of the microPET scanner, where the highest image resolution and sensitivity are available. The microPET studies were performed by tail-vein injection of 3.7 MBq (100 μCi) of ^{18}F-FRGD2 under isoflurane anesthesia. The 60-min dynamic (5×60 s, 5×120 s, 5×180 s, 6×300 s) microPET data acquisition (total of 21 frames) was started 3 min after radiotracer injection. Static images at 2- and 3-h time points were also acquired as 10-min static images. The images were reconstructed by a 2-dimensional ordered-subsets expectation maximum (OSEM) algorithm. No correction was necessary for attenuation or scatter.

Image Analysis

For each microPET scan, regions of interest (ROIs) were drawn over each tumor, normal tissue, and major organs by using the ASI Pro 5.2.4.0 program (Concorde Microsystems Inc.) on decay-corrected, whole-body coronal images. The maximum radioactivity concentration (accumulation) within a tumor or an organ was obtained from mean pixel values within the multiple ROI volume, which were converted to μCi/mL/min by using a calibration constant (*26*). Assuming a tissue density of 1 g/mL, the ROIs were converted to μCi/g/min and then divided by the administered activity to obtain an imaging ROI-derived percentage administered activity per gram of tissue (%ID/g).

The dynamic PET data were used for both tracer kinetic modeling and human dosimetry estimation. Graphical analysis (*27,28*) of the PET data used normalized integrated activity in the tumor versus the normalized integrated activity in the muscle (Equation 1). The ratio of integrated tumor uptake divided by tumor uptake was set as the *y*-axis. The ratio of integrated reference tissue uptake divided tumor uptake was set as the *x*-axis of a Logan plot (here we select muscle as reference tissue because of its low integrin expression). The slope of the linear portion of the Logan plot was distribution volume ratio (DVR). The binding potential (BP) = DVR − 1.

$$\frac{\int_0^T C_t(t)dt}{C_t(T)} = DVR \times \frac{\int_0^T C_r(t)dt}{C_t(T)} + C. \qquad \text{Eq. 1}$$

Quantitation of Tumor Integrin Level

Tumor-bearing mice were sacrificed 24 h after dynamic microPET. The quantitation of tumor tissue integrin level was performed by incubating Nonidet P-40 (NP-40; GE Healthcare)–solubilized tumor tissue lysate with ^{125}I-echistatin in the presence of increasing concentrations of nonradiolabeled echistatin (*29*). Tumor tissue integrin expressions were then quantified by sodium dodecyl sulfate polyacrylamide gel electrophoresis (SDS-PAGE) and autoradiography. Briefly, solubilized tumor tissues were obtained by addition of 0.1 mL/cm^2 of lysis buffer (0.05 mol/L HEPES [pH 7.4], 1% NP-40, 1 mmol/L $CaCl_2$, and 1 mmol/L $MgCl_2$). After incubating on ice for 10–20 min, the samples were collected and centrifuged at 15,000 rpm for 3 min. The resulting solution was then analyzed for total protein content by a Micro BCA (bicinchoninic acid) protein assay (Pierce Biotechnologies). Samples were assayed in triplicate. Twenty micrograms of proteins were incubated in a final volume of 25 μL in binding buffer in the presence of 1.85 kBq of ^{125}I-echistatin and various amounts of echistatin (1–100 nmol/L). After a 2-h incubation at room temperature, the mixtures were loaded onto 4%–10% SDS-PAGE gels. After electrophoresis, the gels were dried and subjected to autoradiograghy overnight. Radioactive bands were developed and quantified in a Cyclone PhosphoImager system (Perkin–Elmer Inc.). The same dose of ^{125}I-echistatin without forming a complex with integrin was used as a standard, and 15 ng of purified integrin $\alpha_v\beta_3$ (Chemicon) was used as a positive control and molecular marker. Each competition curve was then fitted by the Hill equation (GraphPad). The linear portion of the sigmoid curve was used to generate a Scatchard transformation and B_{max} (number of receptors/mg protein).

Statistical Analysis

Quantitative data were expressed as mean ± SD. Means were compared using 1-way ANOVA. The relationship between BP

values and receptor density calculated from SDS-PAGE/autoradiography was evaluated by linear regression and Pearson correlation analyses.

RESULTS

Radiosynthesis

^{18}F-Fluorination of dimeric RGD (E[c(RGDyK)]$_2$) was performed using ^{18}F-SFB (Fig. 1). Synthesis of ^{18}F-SFB followed a previously reported procedure except that ^{18}F-SFB was purified before coupling with an RGD dimer. It was found that the specific activity of ^{18}F-SFB with HPLC purification was higher than that with simple cartridge desalting. The subsequent purification of ^{18}F-FRGD2 was also made easier. The yield of radiochemical acylation was dependent on peptide concentration, temperature, pH, and reaction time. Starting with a $^{18}F^-$ Kryptofix 2.2.2./K_2CO_3 solution, the total reaction time, including final HPLC purification, was about 200 ± 20 min. The maximum overall radiochemical yield with decay correction was 23% ± 2% (n = 20). The radiochemical purity of the labeled peptide was >98% according to analytic HPLC analysis. The specific radioactivity of ^{18}F-SFB was estimated by radio-HPLC to be 200–250 TBq/mmol. Such yield was reached by using 200 μg of E[c(RGDyK)]$_2$ at pH 8.0 and 40°C within 20 min. Note that this yield was significantly lower than that reported for monomeric RGD peptide c(RGDyK), which was >40% (*15,16*).

Quantitation of Tumor Integrin Level

The sigmoid curves for the whole-cell binding assay using ^{125}I-echistatin as radioligand and unlabeled echistatin as competitor were obtained by nonlinear regression fitting of the data using GraphPad Prism. The density of integrin $\alpha_v\beta_3$ receptors on the cell surface was found to be U87MG ≫ NCI-H1975 > MDA-MB-435 > A549 > PC-3 > C6 (Table 1). Quantitation of tumor tissue integrin level by SDS-PAGE/autoradiography, on the other hand, revealed a different order: U87MG > MDA-MB-435 ≫ PC-3 > C6 > NCI-H1975 > A549 (Table 1). A representative autoradiogram of a competition experiment for A549 tumor is shown in Figure 2A. The linear portion of the sigmoid curve (Fig. 2B) was used to generate the Scatchard transformation and the B_{max} (Fig. 2C).

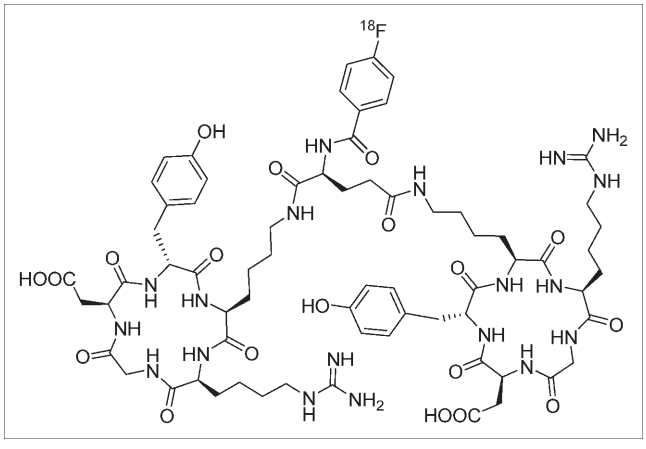

FIGURE 1. Schematic structure of ^{18}F-FB–E[c(RGDyK)]$_2$ (^{18}F-FRGD2).

TABLE 1
Receptor Density for U87MG, MDA-MB-435, C6, PC-3, NCI-H1975, and A549 Tumor Cells Determined by Cell-Binding Assay (n = 3) and Corresponding Tumor Tissues Measured by Ex Vivo SDS-PAGE/Autoradiography

Tumor type	Cell receptor density (no. of receptors/cell)	Tumor receptor density (no. of receptors/mg protein)
U87MG	$(1.28 \pm 0.46) \times 10^5$	4.24×10^{12}
MDA-MB-435	$(1.99 \pm 0.26) \times 10^4$	2.80×10^{12}
C6	$(1.48 \pm 0.28) \times 10^3$	1.51×10^{11}
PC-3	$(2.76 \pm 0.95) \times 10^3$	3.58×10^{11}
NCI-H1975	$(4.42 \pm 0.59) \times 10^4$	2.35×10^{10}
A549	$(1.34 \pm 1.25) \times 10^4$	1.75×10^{10}

Metabolism of ^{18}F-FRGD2

The metabolic stability of ^{18}F-FRGD2 was determined in mouse blood and urine samples and in liver, kidneys, and tumor homogenates 60 min after tracer injection. For all organs, extraction efficiency was between 78% and 93% (Table 2). Between 0.2% and 20% of the total activity could not be trapped on the C_{18} cartridges, which might be attributed to very hydrophilic metabolites or protein-bound activity. The lowest extraction efficiency was found for the U87MG tumor and the highest was found for the blood. HPLC analysis results of the soluble fractions of the different samples are shown in Figure 3. The average fraction of intact tracer was between 80% and 95% (Table 2). The highest metabolic stability of ^{18}F-FRGD2 was found in urine (95.5% intact tracer). Although we did not identify the composition of the metabolites, we found that all of the metabolites eluted earlier from the HPLC column than the parent compound. A minor peak was found at 12 min for all samples. Another metabolite peak was found at about 4 min for the tumor. No defluoridation of ^{18}F-FRGD2 was observed.

PET Study

The dynamic microPET scans were performed for all 6 tumor models. Selected coronal images at different time points after injection of ^{18}F-FRGD2 in a U87MG tumor mouse are shown in Figure 4. High tumor activity accumulation was observed as early as 5 min after injection. Most radioactivity in nontarget tissues was cleared at 70 min after injection. Uptake in the U87MG tumor, kidneys, liver, and lung was 3.81 ± 0.80, 2.25 ± 0.43, 1.10 ± 0.22, and 0.59 ± 0.18 %ID/g, respectively. Time–activity curves showed that this tracer excreted predominantly through the renal route (Fig. 5A). Diversified tumor uptake patterns of ^{18}F-FRGD2 were found in different xenograft models

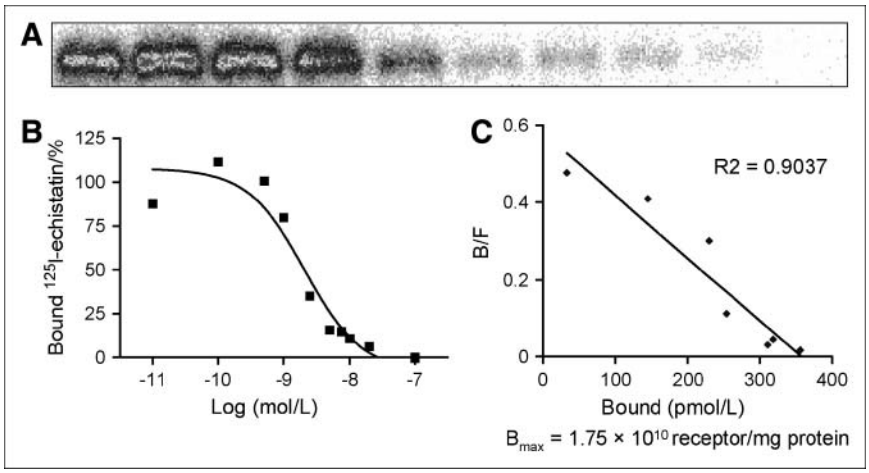

FIGURE 2. Analysis of non–small cell lung cancer A549 tumor tissue integrin level by SDS-PAGE/autoradiography. NP-40–solubilized tumor tissue lysate (30 μg) was incubated with 1×10^5 cpm of ^{125}I-echistatin for 2 h and increasing concentrations of echistatin. After separation on 0.6% SDS-PAGE, an autoradiogram was obtained (A) and each radioactivity band was quantified by using a PhosphoImager system (B). Scatchard transformation of the sigmoid curve generated tissue receptor density (number of receptors/mg tissue) (C).

(Fig. 5B). The U87MG tumor had the highest tumor tissue integrin and tumor cell integrin levels and also had the highest initial tumor uptake but also had the most rapid tumor washout, reaching a plateau after 50 min following injection. The tumors with low magnitude of tumor uptake had minimal tumor washout, providing reasonably high tumor contrast at late time points when nonspecific activity accumulation in the normal organs had been mostly cleared.

Tracer Kinetic Modeling and Correlation Analysis

The Logan plot is a graphical method of analysis, applicable to ligands that bind reversibly to receptors or enzymes (*27,28*). This method can calculate the distribution volume for dynamic PET data before steady state is actually reached. We used 26.5 min as the starting point for linear regression of the dynamic microPET studies because all graphs became linear after that point, with the slope being DVR (Fig. 5C). The calculated BP (B_{max}/K_d) (K_d is dissociation constant) for ^{18}F-FRGD2 in the U87MG, MDA-MB-435, C6, PC-3, NCI-H1975, and A549 tumors using muscle as reference tissue was found to be 29.5, 17.5, 5.8, 1.9, 4.1, and 3.8, respectively.

A linear relationship was found between the BP values calculated from graphical analysis of dynamic microPET and the B_{max} values measured from SDS-PAGE/autoradiograms ($R^2 = 0.96$; $P = 0.005$) (Fig. 6A). The tumor-to-contralateral background ratios did not provide the same level of correlation with the tumor tissue integrin density at early time points (e.g., Pearson correlation coefficient R^2 was 0.86 at 5 min and 0.88 at 30 min after injection.) (Figs. 6C and 6D). At 1 h after injection, a good linear relationship was found between the tumor-to-background ratio and the tumor integrin level (Fig. 6E). Interestingly, the tumor cell integrin level did not have the same level of correlation with tumor contrast or BP (Figs. 6B and 6F).

TABLE 2
Extraction Efficiency and Elution Efficiency Data and HPLC Analysis of Soluble Fraction of Tissue Samples at 60 Minutes After Injection

Fraction	Blood	Urine	Liver	Kidney	U87MG
	Extraction efficiency (%)				
Unsoluble fraction*	6.9	ND	12.6	16.5	21.7
Soluble fraction†	93.1	ND	87.4	83.5	78.3
	Elution efficiency (%)				
Nonretained fraction‡	2.1	0.2	37.1	14.5	15.2
Wash water§	0.6	0.7	3.0	1.6	3.0
Acetonitrile eluent¶	97.2	99.1	59.9	83.8	81.8
	HPLC analysis (%)				
Intact tracer	90.6	95.5	93.5	87.8	79.9

*Amount of activity that was retained in pellets.
†Amount of activity that was extracted to PBS solution.
‡Amount of activity that could not be trapped on C_{18} cartridge.
§Amount of activity that was eluted from C_{18} cartridge using 2 mL water.
¶Amount of activity that was eluted from C_{18} cartridge using 2 mL acetonitrile with 0.1% TFA.
ND = not determined.

DISCUSSION

Monomeric RGD peptide c(RGDyV) was first labeled by Haubner et al. with ^{125}I (*30*). This relatively lipophilic compound had rapid tumor washout and unfavorable hepatobiliary excretion. The resulting high liver and intestinal activity accumulation limited its further application. Glycosylation of the RGD peptide decreased the lipophilicity and, consequently, the hepatic uptake (*31*). The same glycopeptide was then labeled with ^{18}F via the (±)-2-^{18}F-fluoropropionate prosthetic group (*17–19*). The so-called ^{18}F-galacto–RGD demonstrated integrin $\alpha_v\beta_3$–specific tumor uptake in the integrin-positive M21 melanoma xenograft model. Initial clinical trials in healthy volunteers and a limited number of cancer patients revealed that this tracer can be administered safely to patients and is capable of delineating certain lesions that are integrin positive (*19*). The

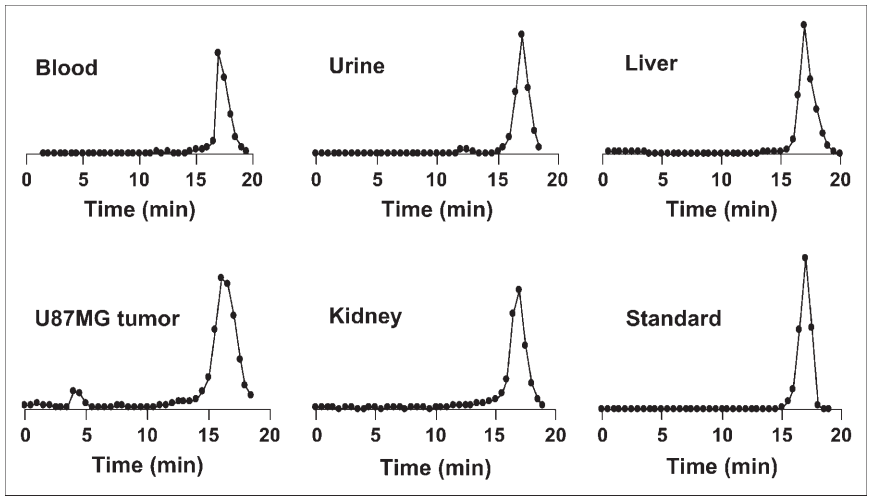

FIGURE 3. Representative HPLC profiles of the reference compound ^{18}F-FRGD2, the soluble fractions of blood and urine samples, tumor, kidney, and liver homogenates collected 1 h after tracer injection. Dimeric RGD peptide tracer is metabolically stable in most organs and tissues.

Wilcoxon signed rank test showed that RGD/PET standardized uptake value (SUV) analysis might be related to tumor vessel density (CD31 staining). Despite the initial success of this tracer in preclinical and clinical studies, several unresolved issues diminished the enthusiasm. A more appropriate RGD peptide probe will almost certainly be required. As a monomeric RGD peptide tracer, ^{18}F-galacto–RGD had relatively low integrin-binding affinity and, thus, only moderate tumor SUVs (*18,19*). Although glycosylation improved the pharmacokinetic behavior of an otherwise hydrophobilic RGD peptide tracer, prominent activity accumulation in the kidneys, spleen, liver, and intestines was still found in both preclinical animal models and human studies. Furthermore, it is not clear whether the tumor contrast from ^{18}F-galacto–RGD/PET is a true reflection of the level of tumor integrin $\alpha_v\beta_3$ expression in vivo.

To correlate $\alpha_v\beta_3$ expression and tumor uptake of ^{18}F-galacto–RGD, subcutaneous tumor models were produced by inoculating a mixed population of M21 (integrin positive) and M21-L (integrin negative) cells. The tumor-to-background ratios obtained from PET and the tumor-to-muscle ratios obtained from direct tissue sampling were then compared with relative α_v integrin expression measured by Western blot analysis under a reducing condition. Relatively poor correlation was found (Pearson correlation coefficient R^2 was around 0.56). Initial clinical translation of this tracer also gave mixed results. A patient with a stage IV malignancy and multiple metastases in liver, skin, and lower abdomen had marked uptake of ^{18}F-FDG but failed to have any ^{18}F-galacto–RGD (*19*). Because the tumor sections were not validated by immunohistochemical staining, it is unclear whether these lesions are integrin negative or the tracer is insensitive.

Because the monomeric RGD pentapeptide in a bent conformation has been optimized to fit into the deep cleft between the α- and β-units of integrin $\alpha_v\beta_3$ (*32*), it is very unlikely that one can significantly improve integrin affinity and selectivity of the monomeric RGD peptide by fine tuning the pentapeptide configuration. Thus, we and others applied a polyvalency effect (*22–25,33,34*) to develop dimeric and multimeric RGD peptides, with repeating cyclic pentapeptide units connected by glutamates. Initial evaluation of the dimeric RGD peptide tracer ^{18}F-FRGD2 in the subcutaneous U87MG glioma model showed excellent tumor integrin-targeting efficacy and favorable in vivo kinetics of this tracer. Although a receptor-blocking experiment demonstrated integrin specificity of the tracer, it is unknown whether the magnitude of tumor uptake is able to document tumor integrin density in vivo. In this study we evaluated the ability of noninvasive PET to quantify the tumor integrin level.

Quantification of cell or tissue integrin $\alpha_v\beta_3$ expression by immunoblotting is technically challenging because of

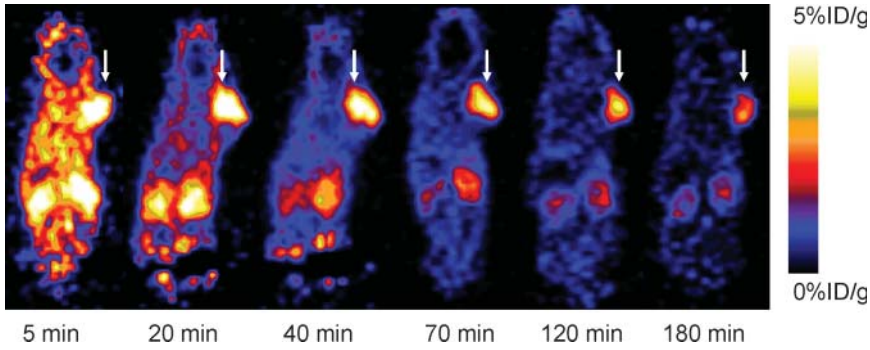

FIGURE 4. Dynamic microPET study of U87MG tumor-bearing mouse over 60 min after injection of ^{18}F-FRGD2 (3.7 MBq [100 μCi]), static scans at 2- and 3-h time points were also conducted to complete the tracer kinetic study. Decay-corrected, whole-body coronal images that contain the tumor are shown. (Reprinted with permission of BioTechniques to reproduce parts of Figure 6.)

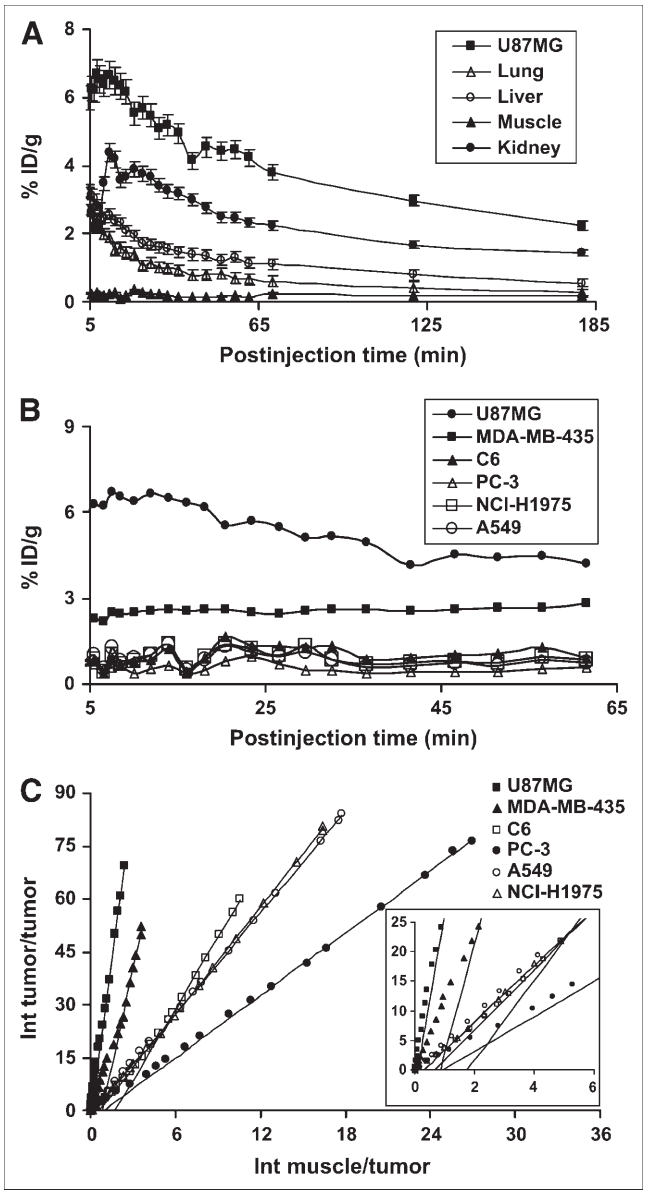

FIGURE 5. (A) Time–activity curves derived from 60-min dynamic and 70-min, 120-min, and 180-min static microPET study. ROIs are shown as mean %ID/g ± SD (n = 3). (B) Comparison of tumor uptake in nude mice derived from 60-min dynamic microPET scans. (C) Logan plots derived from 60-min dynamic microPET data, which showed excellent linearity of normalized integrated (Int) tumor activity vs. normalized integrated muscle tissue activity effective for time >25 min. Slopes of fits represent DVRs. (Reprinted with permission of BioTechniques to reproduce parts of Figure 6.)

the heterodimeric feature of this G-protein receptor. Both anti-α_v and anti-β_3 antibodies are thus needed to confirm the presence of integrin $\alpha_v\beta_3$ and, yet, it is difficult to be quantitative (*35*). It was recently reported that ^{125}I-echistatin forms an SDS-stable complex with certain integrins (resistant to 0.6% SDS) in the absence of chemical cross-linkers, reducing conditions, and heating (*29*). We only detected a single radioactive band for all of the tumor tissue lysates tested. On the basis of the cross-reactivity of this band with selective anti-α- and β-subunit antibodies, it is suggested that ^{125}I-echistatin binds to $\alpha_v\beta_3$. A control experiment with pure integrin $\alpha_v\beta_3$, $\alpha_v\beta_5$, and $\alpha_5\beta_1$ proteins also indicated that the single band detected from cell and tissue lysates is $\alpha_v\beta_3$ (data not shown). Based on the 6 tumor models tested, the BP derived from tracer kinetic analysis correlated well with the tumor integrin expression level measured by SDS-PAGE/autoradiography. To our knowledge, this is the first report that one can quantify integrin expression in vivo by noninvasive PET, which provides the basis for precise documentation of tumor integrin levels without biopsy. It is also worth mentioning that the tumor-to-background ratio at 60 min after injection had better correlation with tumor integrin levels that those at 5 and 30 min after injection. (Figs. 6C–6E), presumably due to the presence of nonspecific uptake, such as perfusion and vascular permeability at early time points. Tumor contrast had a considerable correlation with the tumor tissue integrin level at late time points. Overall, tracer kinetic modeling allows a better quantitative measurement of $\alpha_v\beta_3$ expression by PET. It is likely that the tumor-to-background or tumor-to-muscle ratios reported by Haubner et al. in their melanoma tumor model with mixed population of M21 and M21-L cells might have been more positively correlated with tumor integrin levels if the dissected tumors were quantified by SDS-PAGE/autoradiography instead of Western blots. The sample size in this study is rather low. We tested only 6 tumor models. More animal models (subcutaneous, orthotopic, and even transgenic) at different stages of tumor growth are needed to further validate the Pearson correlation analysis and to determine whether tracer kinetic modeling is superior to tumor-to-background contrast. It would be clinically more advantageous to have a good correlation between tumor-to-background ratios or SUVs and tumor integrin expression level quantified by receptor autoradiography, as documentation of the patient integrin level may be obtained without dynamic scans.

We also note that neither the BP values calculated from the Logan plot nor the tumor-to-background contrast quantified from microPET had a good linear relationship with tumor cell integrin levels measured by the receptor-binding assay. It is well-documented that integrin $\alpha_v\beta_3$ is expressed not only on a variety of tumor cells but also is present at a high level on activated endothelial cells during angiogenesis. The integrin expression on tumor cells grown in tissue culture does not necessarily reflect the tumor tissue integrin level. For example, SDS-PAGE/autoradiography analysis of MDA-MB-435 breast cancer cell lysates and tissue lysates found that the tumor tissue integrin level is about 4- to 5-fold higher than that of tumor cells, indicating that integrin $\alpha_v\beta_3$ expressed on newly developed neovasculatures tends to be much higher than that on the tumor cells (data not shown).

The Logan plot is applicable to the tracers that are reversible, whereas Patlak analysis (*36*) is good for tracers

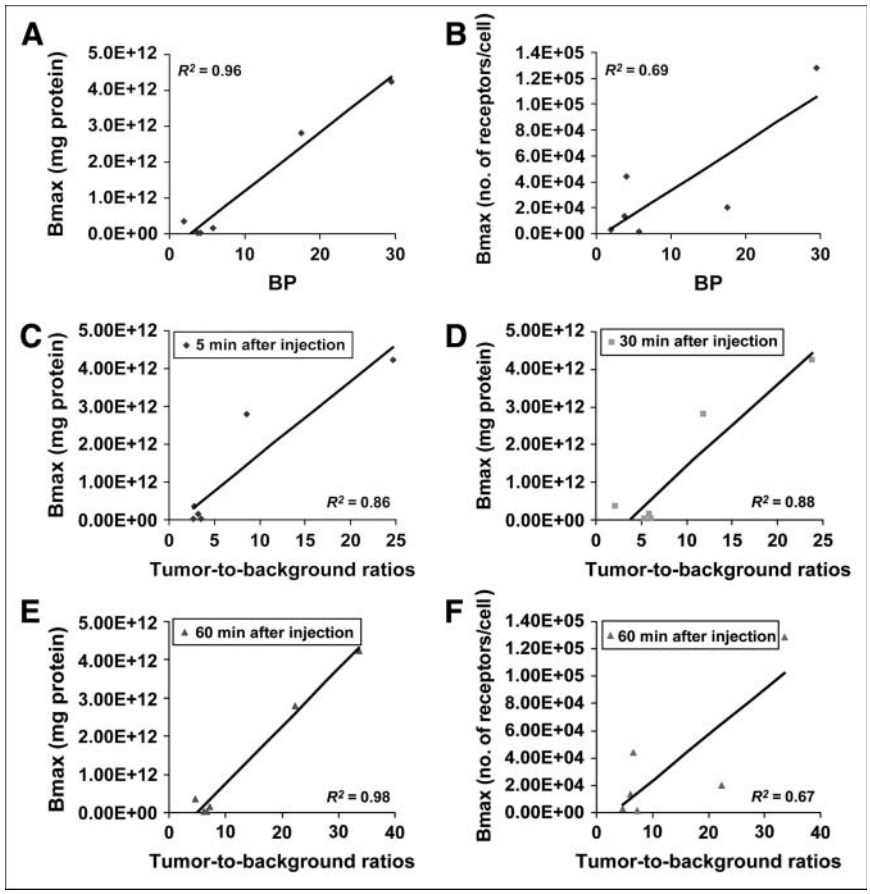

FIGURE 6. Correlation analysis is shown between tumor tissue receptor density (number of receptors/mg protein measured from SDS-PAGE/autoradiography using ^{125}I-echistatin as radioligand) vs. BP (calculated from Logan plot transformation of dynamic microPET data) ($R^2 = 0.96$) (A); tumor cell integrin expression (number of receptors/cell measured from whole-cell receptor-binding assay) vs. BP ($R^2 = 0.69$) (B); tumor tissue receptor density vs. tumor-to-background ratios (calculated from time–activity curves derived from dynamic microPET). Coefficient of determination R^2 is about 0.86, 0.87, and 0.98 at 5, 30, and 60 min after injection of ^{18}F-FRGD2, respectively (C–E); tumor cell receptor density vs. tumor-to-background ratio at 60 min after injection of ^{18}F-FRGD2. Coefficient of determination R^2 is 0.67 (F). Data derived from 6 tumor models (U87MG, C6, MDA-MB-435, PC-3, NCI-H1975, and A549) illustrate excellent linear relationship between tumor tissue receptor density vs. BP and tumor tissue receptor density vs. tumor-to-background ratio at 1 h after injection. (Reprinted with permission of BioTechniques to reproduce parts of Figure 6.)

that are irreversible. We actually performed both Logan plot and Patlak analysis for all dynamic PET data. The Patlak curves deflected downward for the later time points, which is probably a good indication that the tracer is actually reversible. The effectiveness of the blocking of tracer uptake by unlabeled RGD peptide in a dose-dependent manner provides further evidence of the reversible receptor binding of this tracer. A flat curve of some tumor types shown in Figure 5B may still be slowly reversible, in which it may not be so evident by visual inspection of the curve shapes over 60 min. Therefore, quantification of integrin expression level by noninvasive PET may provide a unique way of documenting tumor angiogenesis, in analogy to other established tracers such as FDG for tumor metabolism, radiolabeled antibodies for cell-surface antigen, and suitably labeled annexin V for apoptosis imaging studies.

The optimized coupling yield for the dimeric RGD peptide is significantly lower than that for the monomeric RGD peptide and other peptides reported in the literature using ^{18}F-SFB as synthon. The monomer with a lysine side-chain ε-amino group has much less steric hindrance and a higher pK_a value than a glutamate α-amino group and is, thus, more easily derivatized. Introduction of a linker to the glutamate amine will not only serve as a pharmacokinetic modifier but also modifies the flexibility and acidity of the terminal amine group for ^{18}F-SFB incorporation. A further structure–activity study is required to determine whether an appropriate amino acid linker to $E[c(RGDyK)]_2$ will improve the radiolabeling yield without compromising the tumor targeting efficacy and in vivo kinetics of ^{18}F-FRGD2.

CONCLUSION

This study demonstrates that ^{18}F-labeled dimeric RGD peptide ^{18}F-FRGD2 has initial high activity accumulation in $\alpha_v\beta_3$-integrin–rich tumors and has some washout with time, providing high tumor-to-background ratio even at early time points. ^{18}F-FRGD2 uptake in tumors with medium or low $\alpha_v\beta_3$ levels was also low but minimal tumor washout was observed, and consequently clear tumor contrast is observable at late time points. The binding potential calculated from graphical analysis of dynamic PET data is a better indicator than the tumor-to-background contrast for tumor integrin level in various preclinical tumor models.

ACKNOWLEDGMENTS

This work was supported, in part, by National Institute of Biomedical Imaging and Bioengineering grant R21 EB001785, Department of Defense (DOD) Breast Cancer Research Program (BCRP) Concept award DAMD17-03-1-0752, DOD BCRP IDEA award W81XWH-04-1-0697, DOD Prostate Cancer Research Program New Investigator

award DAMD1717-03-1-0143, the American Lung Association California, the Society of Nuclear Medicine Education and Research Foundation, National Cancer Institute (NCI) Small Animal Imaging Resource Program grant R24 CA93862, and NCI In Vivo Cellular Molecular Imaging Center grant P50 CA114747.

REFERENCES

1. Danen EH. Integrins: regulators of tissue function and cancer progression. *Curr Pharm Des.* 2005;11:881–891.
2. Hynes RO. Integrins: bidirectional, allosteric signaling machines. *Cell.* 2002; 110:673–687.
3. De S, Razorenova O, McCabe NP, et al. VEGF-integrin interplay controls tumor growth and vascularization. *Proc Natl Acad Sci U S A.* 2005;102:7589–7594.
4. Robinson SD, Reynolds LE, Wyder L, et al. β_3-Integrin regulates vascular endothelial growth factor-A-dependent permeability. *Arterioscler Thromb Vasc Biol.* 2004;24:2108–2114.
5. Friedlander M, Brooks PC, Shaffer RW, et al. Definition of two angiogenic pathways by distinct α_v integrins. *Science.* 1995;270:1500–1502.
6. Kumar CC. Integrin $\alpha_v\beta_3$ as a therapeutic target for blocking tumor-induced angiogenesis. *Curr Drug Targets.* 2003;4:123–131.
7. Haubner R, Wester HJ. Radiolabeled tracers for imaging of tumor angiogenesis and evaluation of anti-angiogenic therapies. *Curr Pharm Des.* 2004;10: 1439–1455.
8. Dayton PA, Pearson D, Clark J, et al. Ultrasonic analysis of peptide- and antibody-targeted microbubble contrast agents for molecular imaging of $\alpha_v\beta_3$-expressing cells. *Mol Imaging.* 2004;3:125–134.
9. Ellegala DB, Leong-Poi H, Carpenter JE, et al. Imaging tumor angiogenesis with contrast ultrasound and microbubbles targeted to $\alpha_v\beta_3$. *Circulation.* 2003;108: 336–341.
10. Leong-Poi H, Christiansen J, Klibanov AL, et al. Noninvasive assessment of angiogenesis by ultrasound and microbubbles targeted to α_v-integrins. *Circulation.* 2003;107:455–460.
11. Sipkins DA, Cheresh DA, Kazemi MR, et al. Detection of tumor angiogenesis in vivo by $\alpha_v\beta_3$-targeted magnetic resonance imaging. *Nat Med.* 1998;4:623–626.
12. Wang W, Ke S, Wu Q, et al. Near-infrared optical imaging of integrin $\alpha_v\beta_3$ in human tumor xenografts. *Mol Imaging.* 2004;3:343–351.
13. Chen X, Conti PS, Moats RA. In vivo near-infrared fluorescence imaging of integrin $\alpha_v\beta_3$ in brain tumor xenografts. *Cancer Res.* 2004;64:8009–8014.
14. Chen X. Multimodality imaging of tumor integrin expression. *Mini Rev Med Chem.* In press.
15. Chen X, Park R, Shahinian AH, et al. ^{18}F-Labeled RGD peptide: initial evaluation for imaging brain tumor angiogenesis. *Nucl Med Biol.* 2004;31:179–189.
16. Chen X, Park R, Tohme M, et al. MicroPET and autoradiographic imaging of breast cancer α_v-integrin expression using ^{18}F- and ^{64}Cu-labeled RGD peptide. *Bioconjug Chem.* 2004;15:41–49.
17. Haubner R, Wester HJ, Weber WA, et al. Noninvasive imaging of $\alpha_v\beta_3$ integrin expression using ^{18}F-labeled RGD-containing glycopeptide and positron emission tomography. *Cancer Res.* 2001;61:1781–1785.
18. Haubner R, Kuhnast B, Mang C, et al. [^{18}F]Galacto-RGD: synthesis, radiolabeling, metabolic stability, and radiation dose estimates. *Bioconjug Chem.* 2004;15:61–69.
19. Haubner R, Weber WA, Beer AJ, et al. Noninvasive visualization of the activated $\alpha_v\beta_3$ integrin in cancer patients by positron emission tomography and [^{18}F]galacto-RGD. *PLOS Med.* [serial online]. 2005;2:e70. Accessed March 29, 2005.
20. Chen X, Park R, Shahinian AH, et al. Pharmacokinetics and tumor retention of ^{125}I-labeled RGD peptide are improved by PEGylation. *Nucl Med Biol.* 2004; 31:11–19.
21. Chen X, Park R, Hou Y, et al. MicroPET imaging of brain tumor angiogenesis with ^{18}F-labeled PEGylated RGD peptide. *Eur J Nucl Med Mol Imaging.* 2004;31:1081–1089.
22. Chen X, Plasencia C, Hou Y, et al. Synthesis and biological evaluation of dimeric RGD peptide-paclitaxel conjugate as a model for integrin-targeted drug delivery. *J Med Chem.* 2005;48:1098–1106.
23. Chen X, Sievers E, Hou Y, et al. Integrin $\alpha_v\beta_3$-targeted imaging of lung cancer. *Neoplasia.* 2005;7:271–279.
24. Chen X, Tohme M, Park R, et al. Micro-PET imaging of $\alpha_v\beta_3$-integrin expression with ^{18}F-labeled dimeric RGD peptide. *Mol Imaging.* 2004;3:96–104.
25. Chen X, Liu S, Hou Y, et al. MicroPET imaging of breast cancer α_v-integrin expression with ^{64}Cu-labeled dimeric RGD peptides. *Mol Imaging Biol.* 2004; 6:350–359.
26. Wu Y, Zhang X, Xiong Z, et al. microPET imaging of glioma integrin $\alpha_v\beta_3$ expression using ^{64}Cu-labeled tetrameric RGD peptide. *J Nucl Med.* 2005;46: 1707–1718.
27. Logan J. Graphical analysis of PET data applied to reversible and irreversible tracers. *Nucl Med Biol.* 2000;27:661–670.
28. Logan J. A review of graphical methods for tracer studies and strategies to reduce bias. *Nucl Med Biol.* 2003;30:833–844.
29. Thibault G. Sodium dodecyl sulfate-stable complexes of echistatin and RGD-dependent integrins: a novel approach to study integrins. *Mol Pharmacol.* 2000; 58:1137–1145.
30. Haubner R, Wester HJ, Reuning U, et al. Radiolabeled $\alpha_v\beta_3$ integrin antagonists: a new class of tracers for tumor targeting. *J Nucl Med.* 1999;40:1061–1071.
31. Haubner R, Wester HJ, Burkhart F, et al. Glycosylated RGD-containing peptides: tracer for tumor targeting and angiogenesis imaging with improved biokinetics. *J Nucl Med.* 2001;42:326–336.
32. Xiong JP, Stehle T, Zhang R, et al. Crystal structure of the extracellular segment of integrin $\alpha_v\beta_3$ in complex with an Arg-Gly-Asp ligand. *Science.* 2002;296: 151–155.
33. Janssen ML, Oyen WJ, Dijkgraaf I, et al. Tumor targeting with radiolabeled $\alpha_v\beta_3$ integrin binding peptides in a nude mouse model. *Cancer Res.* 2002; 62:6146–6151.
34. Janssen M, Oyen WJ, Massuger LF, et al. Comparison of a monomeric and dimeric radiolabeled RGD-peptide for tumor targeting. *Cancer Biother Radiopharm.* 2002;17:641–646.
35. Wong NC, Mueller BM, Barbas CF, et al. Alphav integrins mediate adhesion and migration of breast carcinoma cell lines. *Clin Exp Metastasis.* 1998;16:50–61.
36. Kawatsu S, Kato T, Nagano-Saito A, Hatano K, Ito K, Ishigaki T. New insight into the analysis of 6-[^{18}F]fluoro-L-DOPA PET dynamic data in brain tissue without an irreversible compartment: comparative study of the Patlak and Logan analyses. *Radiat Med.* 2003;21:47–54.